DOI: 10.1002/((please add manuscript number))

Article type: Communication

Control of domain structures in multiferroic thin films through defect engineering

*Linze Li, Jacob R. Jokisaari, Yi Zhang, Xiaoxing Cheng, Xingxu Yan, Colin Heikes, Qiyin Lin, Chaitanya Gadre, Darrell Schlom, Long-Qing Chen, and Xiaoqing Pan**

Dr. L. Z. Li, Dr. Y. Zhang, Dr. X. X. Yan, C. Gadre, Prof. X. Q. Pan

Department of Chemical Engineering and Materials Science, University of California - Irvine, Irvine, CA 92697, USA

E-mail: xiaoqing.pan@uci.edu

Dr. J. R. Jokisaari

Department of Materials Science and Engineering, University of Michigan, Ann Arbor, MI 48109, USA

X. X. Cheng, Prof. L.Q. Chen

Department of Materials Science and Engineering, Penn State University, University Park, PA 16802, USA

Dr. C. Heikes, Prof. D. G. Schlom

Department of Materials Science and Engineering, Cornell University, Ithaca, NY 14853, USA

Dr. Q. Y. Lin, Prof. X. Q. Pan

Irvine Materials Research Institute, University of California - Irvine, Irvine, CA 92697, USA

Prof. D. G. Schlom

Kavli Institute at Cornell for Nanoscale Science, Ithaca, NY 14853, USA

Prof. X. Q. Pan

Department of Physics and Astronomy, University of California - Irvine, Irvine, CA 92697, USA

[+] L. Z. L. and J. R. J. contributed equally to this work

Keywords: ferroelectrics, multiferroics, domain control, defects

Abstract

Domain walls (DWs) have become an essential component in nanodevices based on ferroic thin films. The domain configuration and DW stability, however, are strongly dependent on the boundary conditions of thin films, which makes it difficult to create complex ordered patterns of DWs. Here, we show that novel domain structures, that are otherwise unfavorable under the natural boundary

conditions, can be realized by utilizing engineered nanosized structural defects as building-blocks for reconfiguring DW patterns. It was directly observed that an array of charged defects, which are located within a monolayer thickness, can be intentionally introduced by slightly changing substrate temperature during the growth of multiferroic $BiFeO_3$ thin films. These defects are strongly coupled to the domain structures in the pre-temperature change portion of the $BiFeO_3$ film and can effectively change the configuration of newly grown domains due to the interaction between the polarization and the defects. Thus, two types of domain patterns are integrated into a single film without breaking the DW periodicity. The potential use of these defects for building complex patterns of conductive DWs is also demonstrated.

A domain wall (DWs) is a quasi-2D boundary that separates two states that differ in the orientation of their spontaneous polarization, magnetic moment, or strain. In a ferroelectric material, DWs between areas of differing polarization appear as the material is cooled below the Curie temperature (*Tc*).[1] This occurs as a result of symmetry breaking in the crystal structure during the phase transition, and the domain pattern that forms is governed by minimization of the free energy of the boundaries. The rotation angles between these orientations in neighboring domains are used to define the DW type (*e.g.*, 71°, 109°, and 180°). Over the past few years, there has been increasing evidence showing that DWs can possess functionalities that are absent in the bulk of the domains. Examples include enhanced ferroelectricity and magnetism,[2, 3] increased conductivity and photovoltages,[4, 5] magnetoelectric coupling,[6, 7] and magneto transport properties,[8] all of which make DWs appealing for applications as active elements in future nanodevices.

The presence and spatial distribution of specific types of DWs plays a crucial role in attaining particular properties in a ferroic film, such as conductivity or photoelectricity. For example in $BiFeO_3$,

one of the most widely studied multiferroics, the 180° and 109° DWs are more conductive than the 71° DWs,[4] and a 71°DW shows larger open circuit voltages under illumination than a 109°DW.[5] In a $BiFeO_3$/ferromagnetic heterostructure, the exchange coupling between the antiferromagnetic $BiFeO_3$ and the ferromagnetic overlayer can enable either an exchange enhancement or an exchange bias, depending directly on the type and crystallography of DWs in the $BiFeO_3$ film.[6] To make use of these properties, it is necessary to control the characteristics and configuration of DWs and produce desirable domain structures. Such controlled domain structures will be useful both for the fundamental study of DW properties, and the design of novel nanodevices based on well controlled domain structures and DW characteristics.

In ferroelectric and ferroelastic thin films, patterns of DWs depend strongly on the boundary conditions at the two surfaces or interfaces. First, the lattice mismatch between the film and substrate leads to a biaxial-strain mechanical boundary condition,[9-12] which can be altered by choosing substrates spanning a wide range of lattice parameters.[13-17] Second, the electrical boundary condition is critically dependent on free charge compensation at the interfaces and can be tailored by choosing substrates or epitaxial buffer layers with different conductivities.[18-20] Additional restrictions on the boundary condition can be made by changing the vicinality or atomic termination of the substrates.[21, 22] By modifying these boundary conditions, previous experimental studies have demonstrated the capability to fabricate large monodomains,[17] arrays of flux-closure domain structures,[17, 23, 24] or periodically striped domains[25-28] in ferroelectric and ferroelastic thin films. One of the major limitations of such a method, however, has been that once the variable at the boundary condition is set, such as choice of substrate, further modification to control or alter domain patterns during material synthesis becomes difficult. This reduces the parameter space for creating more

complex structures with ordered DW patterns and thus imposes restrictions on the functionalities of the system.

Defects in ferroelectric oxides can also have a remarkable impact on ferroelectric domain structures. It is well known that some common types of defects, such as dislocations and vacancies, can interact with ferroelectric domains and DWs, pinning metastable polarization configurations. Recently, it was also discovered that impurity defects, another major type of defect with a structure different from the host material, can induce dramatic changes in domain structures of ferroelectric thin films.[29-31] This finding suggests the possibility of using engineered impurity defects in combination with suitable interface boundary conditions to control domain formation and create complex domain structures. Nevertheless, the observed impurity defects in literature are either accidentally formed in the films or coupled to polarization-structure changes within a range of only a few nanometers of the defect.[29-31] The approach of precisely creating ordered patterns of defects that can control the domain structure in the bulk of the film remains unexplored. Here, using a model system of $BiFeO_3$/$TbScO_3$, we demonstrate the fabrication of arrays of atomically-thin charged planar defects in a controlled manner during the film growth and, most critically, the use of these defects as nano-building-blocks to tailor domain patterns and produce novel periodic arrays of mixed-type DWs that are inaccessible by conventional boundary-condition-tuning methods.

Epitaxial $(001)_{PC}$ oriented $BiFeO_3$ films were grown on $(110)_O$ orthorhombic $TbScO_3$ substrates by the same molecular-beam epitaxy (MBE) method described elsewhere,[17] with the $[100]_{PC} \parallel [1\bar{1}0]_O$ and $[010]_{PC} \parallel [001]_O$ directions (the subscripts PC and O are used to represent pseudocubic and orthorhombic indices, respectively). Because of the small anisotropic strain due to the dissimilar symmetry of $(001)_{PC}$ $BiFeO_3$ and $(110)_O$ $TbScO_3$, two rhombohedral ferroelastic variants

(r1 and r4) can form in the $BiFeO_3$films.[17] This leads to the formation of three possible domain structures with good periodicity, including a uniform monodomain structure and two periodic twinning domain structures (Figure 1a) namely: inclined domain stripes separated by 71° DWs oriented in the $(101)_{PC}$ planes or vertical domain stripes separated by 109° DWs oriented in the $(010)_{PC}$ planes. The monodomain or 71° domain structures have a single out-of-plane polarization vector resulting in uniform positive and negative bound charge on opposite surfaces of the film. This bound charge produces a large depolarization field destabilizing the domain structure, unless it can be screened by free charge carriers. It follows that both the monodomain and the 71° domain structures are usually stabilized in $BiFeO_3$ thin films grown on orthorhombic substrates with the insertion of thick (>20 nm) bottom electrodes.[26, 32, 33] In contrast, if the ferroelectric surfaces are uncompensated by free charges, as is the case here where the $BiFeO_3$ films are directly grown on the insulating $TbScO_3$ substrates, the system favors the formation of 109° domain patterns with alternating out-of-plane polarization that can reduce the total electrostatic energy (Figure S1,2).[17]

We found that the typical 109° domain patterns in the $BiFeO_3/TbScO_3$ system can be transformed to 71° domains or a large monodomain by introducing Fe-rich impurity defects during the film growth. Our prior MBE work indicates that a change of substrate temperature during the growth of a $BiFeO_3$film, given a constant bismuth and oxygen overpressure at a fixed Bi:Fe flux ratio, can result in three different products: (I) $BiFeO_3$ + γ-Fe_2O_3 (at a higher than optimal temperature), (II) $BiFeO_3$ (at an optimal temperature), and (III) $BiFeO_3$ + $Bi_2O_{2.5}$ (at a lower than optimal temperature).[34] The presence of the Fe-rich or Bi-rich impurity phases can be detected during growth by *in situ* reflection high-energy electron diffraction (RHEED).[34] In this work, the layer-by-layer growth of a 400 nm thick $BiFeO_3$ film was initiated at a temperature of ~560 °C at the $TbScO_3$

substrate. At approximately 110 nm from the substrate (276 layers) during growth, the temperature was increased by 10 °C and additional spots in the RHEED pattern, that can be indexed to diffraction from (111)-oriented λ-Fe_2O_3, were observed (Figure S3). Upon the appearance of these spots, the substrate temperature was reduced to ~560 °C. The observed RHEED pattern was present for more than 20 layers but had disappeared by the termination of the growth process, after which we saw no sign of non-smooth or non-perovskite phases in the RHEED and no sign of mixed phases appeared in the subsequent *ex situ* measurement using X-ray diffraction (Figure S4).

In this 400 nm as-grown $BiFeO_3$ film, an array of atomically thin linear defects was observed in the $BiFeO_3$ matrix at a nearly constant depth of 110 – 130 nm above the bottom interface of the film, shown by a bright-field diffraction-contrast transmission electron microscopy (TEM) image of the $BiFeO_3/TbScO_3$ heterostructure (Figure 1b). The resolved domain structures in the $BiFeO_3$ film are depicted schematically below the TEM image (Figure 1b). The polarization vector in each domain was confirmed by directly mapping the polarization based on atomic-scale scanning transmission electron microscopy (STEM) images (Figure S5). Notably, a linear defect is observed on each 109° domain that is polarized upward (green color in Figure 1b) and the horizontal dimension of the defect matches exactly with the domain width. Above some of the defects, 71° domains (blue color in Figure 1b) are stabilized with the DWs located in the $(01\bar{1})_{PC}$ planes, which are different from the $(101)_{PC}$-oriented 71°domain stripes previously reported in $BiFeO_3$ thin films grown on orthorhombic substrates.[26] In contrast, the downward polarized domains (yellow color in Figure 1b) in the lower portion of the film are not blocked by the defects and can extend their volume to the upper portion. As a result, a domain transformation from 109° to 71° across the defects is observed, resulting in the formation of novel mixed-type domains containing “head-to-head” positively

charged DWs located exactly at the defects. Periodic ordering of these domain patterns is further confirmed by a piezoresponse force microscopy (PFM) image of the same heterostructure in cross section, in which the defects are not resolvable (Figure 1c). The correspondence between the appearance of each defect and the position of the 109° and 71° domains indicates a strong interaction between the defects and ferroelectric polarization.

The atomic structures and chemical composition of the defects were examined by high-angle annular dark-field (HAADF) STEM imaging and electron energy loss spectroscopy (EELS). Figure 2a shows a HAADF STEM image of a typical linear defect embedded in the $BiFeO_3$ matrix. As there are no other elements introduced during the film growth, the defect should also be composed of Bi, Fe, and O atoms, with the brighter dots in the HAADF image corresponding to the heavier Bi columns, the weaker dots corresponding to the lighter Fe columns, and O columns not visible. This defect is mostly composed of one type of stepped units (indicated by yellow arrows), which have an inclined orientation and are formed from one pair of Bi atoms alternating with two pairs of Fe atoms. Planar units (indicated by green arrows) oriented on the horizontal $(001)_{PC}$ plane of $BiFeO_3$ are also observed, with the structure of one pair of Bi atoms alternating with one pair of Fe atoms. Additionally, there are segments composed of several consecutive pairs of Fe atoms with no Bi atoms in between them (indicated by white arrows). Across the defect, an atomic shift of one half of a pseudocubic unit cell of the $BiFeO_3$ lattice along the $[010]_{PC}$ direction is observed. This shift occurs mainly through atomic rearrangement at the defects, and thus does not induce obvious strain in the $BiFeO_3$ matrix, as shown by the quantitative analysis of the high-resolution HAADF images using geometric phase analysis in Figure S6.

The O K-edge electron energy loss near edges structures (ELNES) for the $BiFeO_3$ matrix and the stepped defect are shown in Figure2b. The most evident difference between the two spectra is in the A peak region from 530 to 538 eV. While a clear splitting of the A peak into two subpeaks, A1 at 532 eV and A2 at 535 eV, is observed in the spectrum of the $BiFeO_3$ matrix, the A2 subpeak is absent in the spectrum of the defect. It has been previously identified that A1stems from hybridization between the O 2*p* and Fe 3*d* states, and A2 from hybridization between the O 2*p* and Bi 5*d* or 6*d* orbitals.[35-37] The absence of A2 in the spectrum of the defect results in a shape of the A peak that is more similar to *γ*-Fe_2O_3.[38] The accumulation of Fe and O at the defects is further supported by EELS spectrum images of a segment of the defect (Figure 2c-e). The same type of stepped units in the observed defects have also been observed in a previous study of Nd- and Ti-doped anti-ferroelectric $BiFeO_3$ by MacLaren *et. al.*.[39, 40] In their proposed defect structure, the iron atoms are coordinated by 6 oxygen atoms in the form of edge-sharing oxygen octahedra, resembling *γ*-Fe_2O_3. With these *γ* -Fe_2O_3-like structures, an excess of anions (more oxygen) should accumulate at the defects and thus introduce net negative charge. Assuming Bi^{3+}, Fe^{3+}, and O^{2-}at the stepped units of the defect, the local charge density is calculated to be of -1.1 C/m^2.

It is apparent that the negative charge accumulation at the defects can cause strong built-in fields pointing to the defects, which could be at the origin of the observed 109° to 71° domain transition. In fact, the same type of charged defects in the Nd- and Ti-doped non-polar, anti-ferroelectric $BiFeO_3$ can even stabilize tetragonally distorted regions with a strong polarization in ~4–5 unit cells at either side of the defects, as shown by MacLaren *et. al.*.[39, 40]. On the other hand, modification of the surface termination layer, occurring when the defects were introduced during the film growth, may also have an impact. Previous studies of the relation between chemical

termination and polarization orientation in $BiFeO_3$ layers suggest that the growth of $BiFeO_3$ on Fe-O_2 terminated surfaces should result in an as-grown state with downward polarization.[41, 42] Here, the local termination change due to the introduction of the Fe-rich defects could exert a similar effect, forcing the polarization on top of the defects into the downward direction and thus facilitating the domain transformation.

Although now we understand that the introduction of the defects in the thin film can induce the observed domain transformation, the reason for the formation of 71° domains on only a few of the defects, rather than on all of them, requires further explanation. We employed phase-field simulations to understand the energetic driving force for the formation of the 71° domains. In the simulation, atomically thin linear defects with a uniform charge density of -1.1 C/m^2 are inserted on top of all upward polarized 109° domains, at a level 100 nm above the bottom interface in 400 nm $BiFeO_3$ thin films, and the effects of chemical termination change at the defects are ignored. Assuming the upward and downward polarized 109° domains in the lower portion of the film have the same width, we calculated landau, electric, elastic, gradient, and total energies of the systems with different lengths of defects (*i.e.*, widths of upward polarized 109° domains). The energy differences are compared among the three metastable domain configurations as shown in Figure 3a, *i.e.*, (1) no 71° domains above the defect, (2) one 71° domain on every other defect, and (3) one 71° domain on each defect.

The changes in bulk landau energy and electric energy between different domain configurations were found to be at least one order of magnitude smaller than the changes in elastic and gradient energy. Thus, we only plot the differences inelastic, gradient, and total energies between cases (2) and (1), or (3) and (1) as a function of defect length in Figure 3b and c,

respectively, where a similar trend in energy changes is observed. Gradient energy is a major component of the domain wall energy, and the area of domain wall is roughly proportional to the total gradient energy. The increase in gradient energy is mostly attributable to the formation of 71° DWs in the system, and its value is nearly constant as the change of the defect length does not alter the DW area. Elastic energy, on the other hand, is domain-size dependent; it is found that a larger 71° domain width (*i.e.*, larger defect length) results in a greater drop inelastic energy. In order to stabilize the 71° domains (total energy difference< 0) the defect length must surpass a critical value, which is ~ 50 nm for domain configuration (2) and ~ 80 nm for domain configuration (3). The higher value for the latter case is because this domain structure has more 71° DWs, which introduces higher gradient energy in the system.

Phase-field simulations explain why most of the observed 71° domains are on defects longer than 50 nm in the 400 nm $BiFeO_3$ film (Figure 1). This knowledge may also be used to further tune the domain structures above the defects. For example, in Figure 3d, we show a dark-field diffraction-contrast TEM image of a 60 nm $BiFeO_3$ film, in which the same type, but shorter (< 30 nm) defects, were introduced at ~20 nm above the interface. While the 109° and 180° domain patterns similar to those in 20 nm $BiFeO_3$ films grown on $TbScO_3$ are observed below the defects,[32] the short defects couldn't stabilize 71° domains and thus produced a large monodomain in the upper portion of the film.

The potential of using these defects for building complex patterns of conductive DWs is illustrated in Figure 4. In a PFM image of a cross-section sample of the 400 nm $BiFeO_3$ film grown on $TbScO_3$ (Figure 4a), we observed ordered domain patterns containing one 71° domain on top of five 109° domains stabilized by the linear defects (Figure 4a). The schematic domain structure for the

highlighted region in Figure 4a is presented in Figure 4b, which includes not only inclined 71° DWs that penetrate from the top surface to the edge of the defects, but also horizontal 71° DWs sitting between the defects. Conductivity mapping of the same area using conductive atomic force microscopy (c-AFM) indicates the conductive nature of all the inclined and horizontal 71° DWs. While conductive vertical or inclined DWs penetrating the thickness of ferroelectric thin films were frequently observed,[43, 44] the horizontal conductive DWs shown here, buried in the bulk film below the surface, have not been previously reported. These DWs provide additional possibilities for engineering ordered configurations of nanoscale conductive channels in multiple preferred directions in a thin-film system.

In conclusion, we have demonstrated that an array of atomically thin defects inserted during film growth can strongly couple to the domain configuration and the stability of particular domain types in $BiFeO_3$ thin films. By using these defects as active nano-building-blocks we have produced periodic 71° domains or large monodomains, that would be expected to be unstable on top of ordered 109° domains under the normal boundary conditions in the $BiFeO_3/TbScO_3$ system. Application of these methods opens a path to controllable fabrication of complex, multilayer domain structures in ferroic and multiferroic materials, providing novel opportunities for studying the exotic properties of DWs and allowing the design strategy for applicable devices to become more flexible. This study also suggests a route to tune material properties through defect engineering, which can be potentially extended to other ferroelectric and multiferroic oxides, opening up the possibility to stabilize domain structures with novel properties that are inaccessible by conventional methods.

Methods

Transmission electron microscopy (TEM):Cross-sectional TEM specimens were prepared by conventional methods of mechanical polishing followed by argon ion milling. STEM HAADF and EELS experiments were carried out on Nion UltraSTEM 200 equipped with C3/C5 corrector and high-energy resolution monochromated EELS system (HERMES) in Irvine Materials Research Institute at the University of California, Irvine. The microscope was operated at 100 kV with convergence semi-angle of 30 mrad and with a beam current of ~100pA. The inner and outer semi-angles of the ADF detector were approximately 70 and 200 mrad, respectively, and the pixel dwell time for the HAADF image was chosen to be 32 µs. A dispersion of 0.3 eV/channel was used and the dwell time was 0.5 s/pixel for acquisition of EELS spectrum. The pre-edge background in each EELS spectrum was removed by power-law function in commercial software package DigitalMicrograph.

*Piezoresponse force microscopy (PFM) and conductive atomic force microscopy (c-AFM)***:** Cross-sectional specimens used for scanning probe measurements were prepared by the same methods as the standard procedure for preparing TEM specimens, and a conductive platinum layer was deposited on the back of the specimen by sputter coating. PFM and c-AFM measurements were carried out on a commercial Asylum Research MFP-3D scanning probe microscope by using Nanosensors PPP-EFM cantilevers and conductive diamond-coated probes, respectively. For the conductive mapping, a bias of 1 V was applied between the tip (grounded) and the sample, anda nominal force of 16N/m was constantly applied at the tip.

High-resolution X-ray diffraction: High resolution reciprocal space mappings (RSM) were measured to study the film structures at room temperature by using a Rigaku Smartlab diffractometer equipped with a Cu $K_{\alpha1}$ source of radiation (λ = 0.15406 nm) and a Ge (220 × 2) monochromator. The symmetrical RSMs around TSO $(220)_o$ and asymmetrical RSMs around TSO $(240)_o$ and $(332)_o$ were measured.

Phase-field simulations: The time dependent Ginzburg-landau (TDGL) equation,

$$\frac{\partial P_i(r,t)}{\partial t} = -L\frac{\delta F}{\delta P_i(r,t)}(i = 1,2,3),$$

was solved in order to obtain the equilibrium domain structure with several embedded charged defects. F is the total free energy, which can be expressed by integration of four energy density over the whole simulation system:

$$F = \int (f_{landau} + f_{elastic} + f_{electric} + f_{gradient})dV.$$

in which the landau free energy (f_{landau}) is defined as $\alpha_1(P_1^2 + P_2^2 + P_3^2) + \alpha_{11}(P_1^4 + P_2^4 + P_3^4) + \alpha_{12}(P_1^2P_2^2 + P_1^2P_3^2 + P_2^2P_3^2)$.[45] The elastic energy ($f_{elastic}$) can be expressed as $\frac{1}{2}C_{ijkl}\epsilon_{ij}\epsilon_{kl}$, where C_{ijkl} is the elastic modulus tensor, ϵ_{ij} is the elastic strain which can be obtained by solving the mechanical equilibrium equation $\sigma_{ij,j} = 0$, whose boundary condition was traction free on the film surface and clamped at some distance into the substrate.[46] The electric energy ($f_{electric}$) is $-\frac{1}{2}E_i(\epsilon_0\kappa_{ij}E_j + P_i)$, where E_i is electric field along i direction, κ_{ij} is the relative dielectric permittivity, P_i is polarization along i direction. The electric energy can be calculated after solving

the Poisson equation $\nabla^2\phi = -\frac{\rho}{\epsilon}$, whose boundary conditions are short circuit conditions for both film top surface and film/substrate interface.[20] The expression for gradient energy ($f_{gradient}$) is $\frac{1}{2}G_{11}(P_{1,1}^2 + P_{1,2}^2 + P_{1,3}^2 + P_{2,1}^2 + P_{2,2}^2 + P_{2,3}^2 + P_{3,1}^2 + P_{3,2}^2 + P_{3,3}^2)$,[47] where G_{11} is the gradient energy coefficient, and $P_{i,j}$ means the derivative of P_i component along the j direction. The general form of gradient energy has more than one coefficient, but due to the lack of parameters, the expression can be simplified to only use G_{11}, and we set the normalized value of G_{11} to 0.6. In the simulation, the charged defect was considered by modifying the local charge density ρ in the Poisson equation, and we assumed a uniform charge density of $-1.1\ C/m^2$ at the defect.

Supporting Information

Supporting Information is available from the Wiley Online Library or from the author.

Acknowledgements

The experimental work was mainly supported by the Department of Energy (DOE) under grant DE-SC0014430 (L.Z.L., J.R.J., Y.Z., X.X.Y., Q.Y. Lin, C. G., and X.Q.P.). The TEM work was conducted at the Irvine Materials Research Institute at University of California, Irvine. The theoretical work at the Pennsylvania State University was supported by the U.S. Department of Energy, Office of Basic Energy Sciences, Division of Materials Sciences and Engineering under Award FG0207ER46417 (X.X.C. and L.Q.C.). Calculations at the Pennsylvania State University were performed on the Cyberstar Linux Cluster funded by the National Science Foundation through grant OCI0821527. The work at Cornell University was supported by the National Science Foundation (Nanosystems Engineering Research Center for Translational Applications of Nanoscale Multiferroic Systems) under grant number EEC-1160504 (C.H., and D.G.S.). This work was performed in part at the Cornell Nanoscale Facility, a member of the National Nanotechnology Coordinated Infrastructure (NNCI), which is supported by the National Science Foundation (Grant ECCS-1542081). We thank Dr. Zhan Zhang from Argonne National Lab for useful discussion of XRD data.

Received: ((will be filled in by the editorial staff))Revised: ((will be filled in by the editorial staff))Published online: ((will be filled in by the editorial staff))

References

[1] S. K. Streiffer, C. B. Parker, A. E. Romanov, M. J. Lefevre, L. Zhao, J. S. Speck, W. Pompe, C. M. Foster, G. R. Bai, *J. Appl. Phys.* **1998**, *83*, 2742.

[2] X. K. Wei, A. K. Tagantsev, A. Kvasov, K. Roleder, C. L. Jia, N. Setter, *Nat. Commun.* **2014**, *5*, 3031.

[3] J. Privratska, V. Janovec, *Ferroelectrics* **1999**, *222*, 23.

[4] J. Seidel, L. W. Martin, Q. He, Q. Zhan, Y. H. Chu, A. Rother, M. E. Hawkridge, P. Maksymovych, P. Yu, M. Gajek, N. Balke, S. V. Kalinin, S. Gemming, F. Wang, G. Catalan, J. F. Scott, N. A. Spaldin, J. Orenstein, R. Ramesh, *Nat. Mater.* **2009**, *8*, 229.

[5] S. Y. Yang, J. Seidel, S. J. Byrnes, P. Shafer, C. H. Yang, M. D. Rossell, P. Yu, Y. H. Chu, J. F. Scott, J. W. Ager, L. W. Martin, R. Ramesh, *Nat. Nanotechnol.* **2010**, *5*, 143.

[6] L. W. Martin, Y. H. Chu, M. B. Holcomb, M. Huijben, P. Yu, S. J. Han, D. Lee, S. X. Wang, R. Ramesh, *Nano Lett.* **2008**, *8*, 2050.

[7] J. Allibe, S. Fusil, K. Bouzehouane, C. Daumont, D. Sando, E. Jacquet, C. Deranlot, M. Bibes, A. Barthelemy, *Nano Lett.* **2012**, *12*, 1141.

[8] Q. He, C. H. Yeh, J. C. Yang, G. Singh-Bhalla, C. W. Liang, P. W. Chiu, G. Catalan, L. W. Martin, Y. H. Chu, J. F. Scott, R. Ramesh, *Phys. Rev. Lett.* **2012**, *108*.

[9] D. G. Schlom, L. Q. Chen, C. B. Eom, K. M. Rabe, S. K. Streiffer, J. M. Triscone, *Annu. Rev. Mater. Res.* **2007**, *37*, 589.

[10] K. J. Choi, M. Biegalski, Y. L. Li, A. Sharan, J. Schubert, R. Uecker, P. Reiche, Y. B. Chen, X. Q. Pan, V. Gopalan, L. Q. Chen, D. G. Schlom, C. B. Eom, *Science* **2004**, *306*, 1005.

[11] C. Ederer, N. A. Spaldin, *Phys. Rev. Lett.* **2005**, *95*, 257601.

[12] D. G. Schlom, L.-Q. Chen, C. J. Fennie, V. Gopalan, D. A. Muller, X. Pan, R. Ramesh, R. Uecker, *MRS Bulletin* **2014**, *39*, 118.

[13] C. Adamo, X. Ke, H. Q. Wang, H. L. Xin, T. Heeg, M. E. Hawley, W. Zander, J. Schubert, P. Schiffer, D. A. Muller, L. Maritato, D. G. Schlom, *Appl. Phys. Lett.* **2009**, *95*, 112504.

[14] I. C. Infante, S. Lisenkov, B. Dupe, M. Bibes, S. Fusil, E. Jacquet, G. Geneste, S. Petit, A. Courtial, J. Juraszek, L. Bellaiche, A. Barthelemy, B. Dkhil, *Phys. Rev. Lett.* **2010**, *105*, 057601.

[15] H. Bea, B. Dupe, S. Fusil, R. Mattana, E. Jacquet, B. Warot-Fonrose, F. Wilhelm, A. Rogalev, S. Petit, V. Cros, A. Anane, F. Petroff, K. Bouzehouane, G. Geneste, B. Dkhil, S. Lisenkov, I. Ponomareva, L. Bellaiche, M. Bibes, A. Barthelemy, *Phys. Rev. Lett.* **2009**, *102*, 217603.

[16] R. J. Zeches, M. D. Rossell, J. X. Zhang, A. J. Hatt, Q. He, C. H. Yang, A. Kumar, C. H. Wang, A. Melville, C. Adamo, G. Sheng, Y. H. Chu, J. F. Ihlefeld, R. Erni, C. Ederer, V. Gopalan, L. Q. Chen, D. G. Schlom, N. A. Spaldin, L. W. Martin, R. Ramesh, *Science* **2009**, *326*, 977.

[17] C. T. Nelson, B. Winchester, Y. Zhang, S. J. Kim, A. Melville, C. Adamo, C. M. Folkman, S. H. Baek, C. B. Eom, D. G. Schlom, L. Q. Chen, X. Q. Pan, *Nano Lett.* **2011**, *11*, 828.

[18] M. F. Chisholm, W. D. Luo, M. P. Oxley, S. T. Pantelides, H. N. Lee, *Phys. Rev. Lett.* **2010**, *105*, 197602.

[19] C. Lichtensteiger, S. Fernandez-Pena, C. Weymann, P. Zubko, J. M. Triscone, *Nano Lett.* **2014**, *14*, 4205.

[20] Y. L. Li, S. Y. Hu, Z. K. Liu, L. Q. Chen, *Appl. Phys. Lett.* **2002**, *81*, 427.

[21] Y. H. Chu, M. P. Cruz, C. H. Yang, L. W. Martin, P. L. Yang, J. X. Zhang, K. Lee, P. Yu, L. Q. Chen, R. Ramesh, *Adv. Mater.* **2007**, *19*, 2662.

[22] H. W. Jang, D. Ortiz, S. H. Baek, C. M. Folkman, R. R. Das, P. Shafer, Y. Chen, C. T. Nelson, X. Pan, R. Ramesh, C. B. Eom, *Adv. Mater.* **2009**, *21*, 817.

[23] C. L. Jia, K. W. Urban, M. Alexe, D. Hesse, I. Vrejoiu, *Science* **2011**, *331*, 1420.

[24] Y. L. Tang, Y. L. Zhu, X. L. Ma, A. Y. Borisevich, A. N. Morozovska, E. A. Eliseev, W. Y. Wang, Y. J. Wang, Y. B. Xu, Z. D. Zhang, S. J. Pennycook, *Science* **2015**, *348*, 547.

[25] S. K. Streiffer, J. A. Eastman, D. D. Fong, C. Thompson, A. Munkholm, M. V. R. Murty, O. Auciello, G. R. Bai, G. B. Stephenson, *Phys. Rev. Lett.* **2002**, *89*, 067601.

[26] Y. H. Chu, Q. He, C. H. Yang, P. Yu, L. W. Martin, P. Shafer, R. Ramesh, *Nano Lett.* **2009**, *9*, 1726.

[27] C. M. Folkman, S. H. Baek, H. W. Jang, C. B. Eom, C. T. Nelson, X. Q. Pan, Y. L. Li, L. Q. Chen, A. Kumar, V. Gopalan, S. K. Streiffer, *Appl. Phys. Lett.* **2009**, *94*, 251911.

[28] Y. H. Chu, Q. Zhan, L. W. Martin, M. P. Cruz, P. L. Yang, G. W. Pabst, F. Zavaliche, S. Y. Yang, J. X. Zhang, L. Q. Chen, D. G. Schlom, I. N. Lin, T. B. Wu, R. Ramesh, *Adv. Mater.* **2006**, *18*, 2307.

[29] L. Z. Li, Y. Zhang, L. Xie, J. R. Jokisaar, C. Beekman, J. C. Yang, Y. H. Chu, H. M. Christen, X. Q. Pan, *Nano Lett.* **2017**, *17*, 3556.

[30] L. Xie, L. Z. Li, C. A. Heikes, Y. Zhang, Z. J. Hong, P. Gao, C. T. Nelson, F. Xue, E. Kioupakis, L. Q. Chen, D. G. Schlom, P. Wang, X. Q. Pan, *Adv. Mater.* **2017**, *29*, 1701475.

[31] L. Z. Li, X. X. Cheng, J. R. Jokisaari, P. Gao, J. Britson, C. Adamo, C. Heikes, D. G. Schlom, L. Q. Chen, X. Q. Pan, *Phys. Rev. Lett.* **2018**, *120*, 137602.

[32] L. Z. Li, P. Gao, C. T. Nelson, J. R. Jokisaari, Y. Zhang, S. J. Kim, A. Melville, C. Adamo, D. G. Schlom, X. Q. Pan, *Nano Lett.* **2013**, *13*, 5218.

[33] L. Z. Li, J. Britson, J. R. Jokisaari, Y. Zhang, C. Adamo, A. Melville, D. G. Schlom, L. Q. Chen, X. Q. Pan, *Adv. Mater.* **2016**, *28*, 6574.

[34] J. F. Ihlefeld, N. J. Podraza, Z. K. Liu, R. C. Rai, X. Xu, T. Heeg, Y. B. Chen, J. Li, R. W. Collins, J. L. Musfeldt, X. Q. Pan, J. Schubert, R. Ramesh, D. G. Schlom, *Appl. Phys. Lett.* **2008**, *92*, 142908.

[35] M. D. Rossell, R. Erni, M. P. Prange, J. C. Idrobo, W. Luo, R. J. Zeches, S. T. Pantelides, R. Ramesh, *Phys. Rev. Lett.* **2012**, *108*, 047601.

[36] T. J. Park, S. Sambasivan, D. A. Fischer, W. S. Yoon, J. A. Misewich, S. S. Wong, *J Phys Chem C* **2008**, *112*, 10359.

[37] R. Saeterli, S. M. Selbach, P. Ravindran, T. Grande, R. Holmestad, *Phys. Rev. B* **2010**, *82*.

[38] J. H. Paterson, O. L. Krivanek, *Ultramicroscopy* **1990**, *32*, 319.

[39] I. MacLaren, L. Q. Wang, O. Morris, A. J. Craven, R. L. Stamps, B. Schaffer, Q. M. Ramasse, S. Miao, K. Kalantari, I. Sterianou, I. M. Reaney, *Apl Mater.* **2013**, *1*, 021102.

[40] I. MacLaren, L. Q. Wang, A. J. Craven, Q. M. Ramasse, B. Schaffer, K. Kalantari, I. M. Reaney, *Apl Mater.* **2014**, *2*, 066106.

[41] P. Yu, W. Luo, D. Yi, J. X. Zhang, M. D. Rossell, C. H. Yang, L. You, G. Singh-Bhalla, S. Y. Yang, Q. He, Q. M. Ramasse, R. Erni, L. W. Martin, Y. H. Chu, S. T. Pantelides, S. J. Pennycook, R. Ramesh, *P. Natl. Acad. Sci.* **2012**, *109*, 9710.

[42] G. De Luca, N. Strkalj, S. Manz, C. Bouillet, M. Fiebig, M. Trassin, *Nat. Commun.* **2017**, *8*, 1419.

[43] J. Seidel, P. Maksymovych, Y. Batra, A. Katan, S. Y. Yang, Q. He, A. P. Baddorf, S. V. Kalinin, C. H. Yang, J. C. Yang, Y. H. Chu, E. K. H. Salje, H. Wormeester, M. Salmeron, R. Ramesh, *Phys. Rev. Lett.* **2010**, *105*, 197603.

[44] S. Farokhipoor, B. Noheda, *Phys. Rev. Lett.* **2011**, *107*, 127601.

[45] J. X. Zhang, D. G. Schlom, L. Q. Chen, C. B. Eom, *Appl. Phys. Lett.* **2009**, *95*, 122904.

[46] Y. L. Li, S. Y. Hu, Z. K. Liu, L. Q. Chen, *Acta Mater.* **2002**, *50*, 395.

[47] J. X. Zhang, Y. L. Li, S. Choudhury, L. Q. Chen, Y. H. Chu, F. Zavaliche, M. P. Cruz, R. Ramesh, Q. X. Jia, *J. Appl. Phys.* **2008**, *103*.

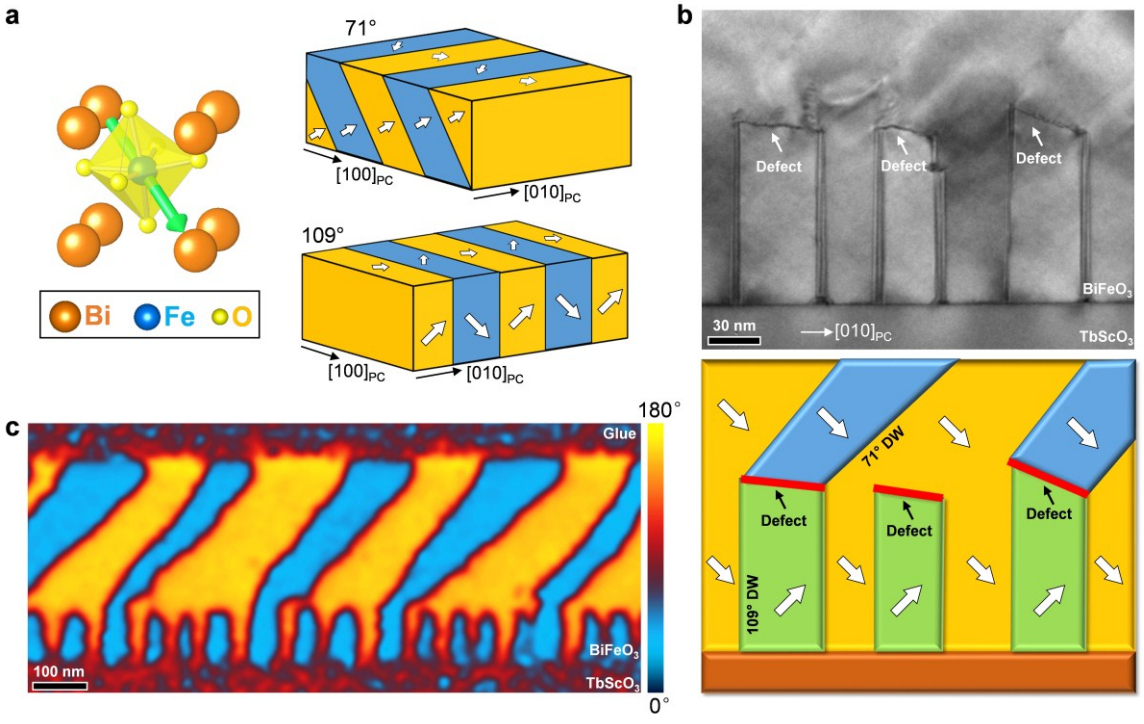

Figure 1. Domain structures in $BiFeO_3$ thin films. **a**, Left, atomic model of $BiFeO_3$ pseudocubic structure (left), polarization is shown by the green arrow. Right, 71° and 109° domain patterns in BFO thin films. Polarizations are shown by white arrows. **b**, Cross-sectional bright-field TEM image and corresponding schematic of polarization structures showing ordered 71° and 109° domains separated by an array of defects in a 400 nm $BiFeO_3$ film. **c**, PFM phase image showing the same periodically ordered domain patterns in the same $BiFeO_3$ film.

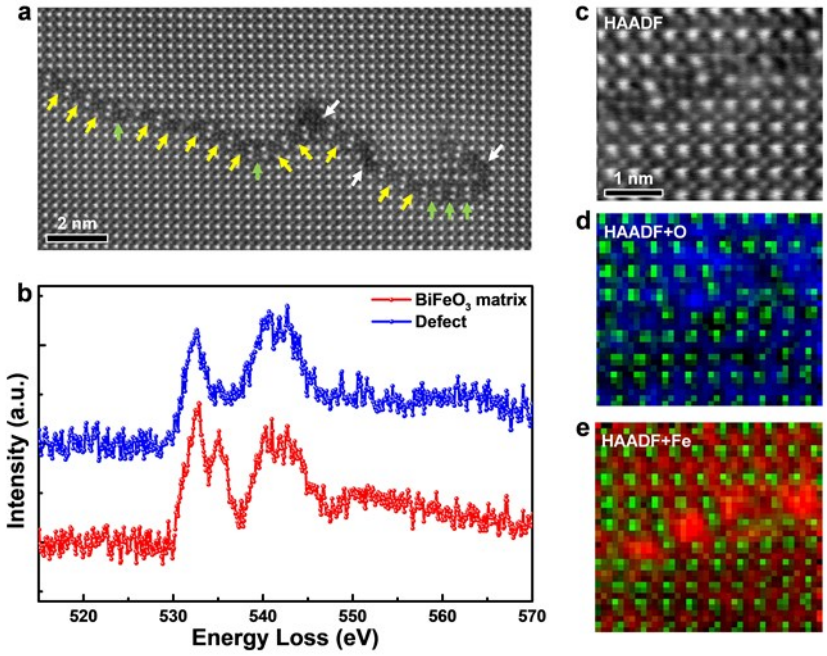

Figure 2. Atomic structures and chemical information at the defects. **a**, Atomic-scale HAADF STEM image of a linear defect inserted in the $BiFeO_3$ matrix. Stepped units on the defect are indicated by the yellow arrows; planar units are indicated by green arrows; and white arrows indicate several defect segments with consecutive pairs of Fe atoms with no Bi atoms in between them. **b**, O-K ELNES of the $BiFeO_3$ matrix and the stepped defect. **c**, HAADF STEM image of a segment on the defect and corresponding spectrum images of the same area: **d**, combined map of O (blue color) and HAADF signal (A-site atoms, *i.e.*, Bi, shown by green color) and **e**, combined map of Fe (red color) and HAADF signal (green color).

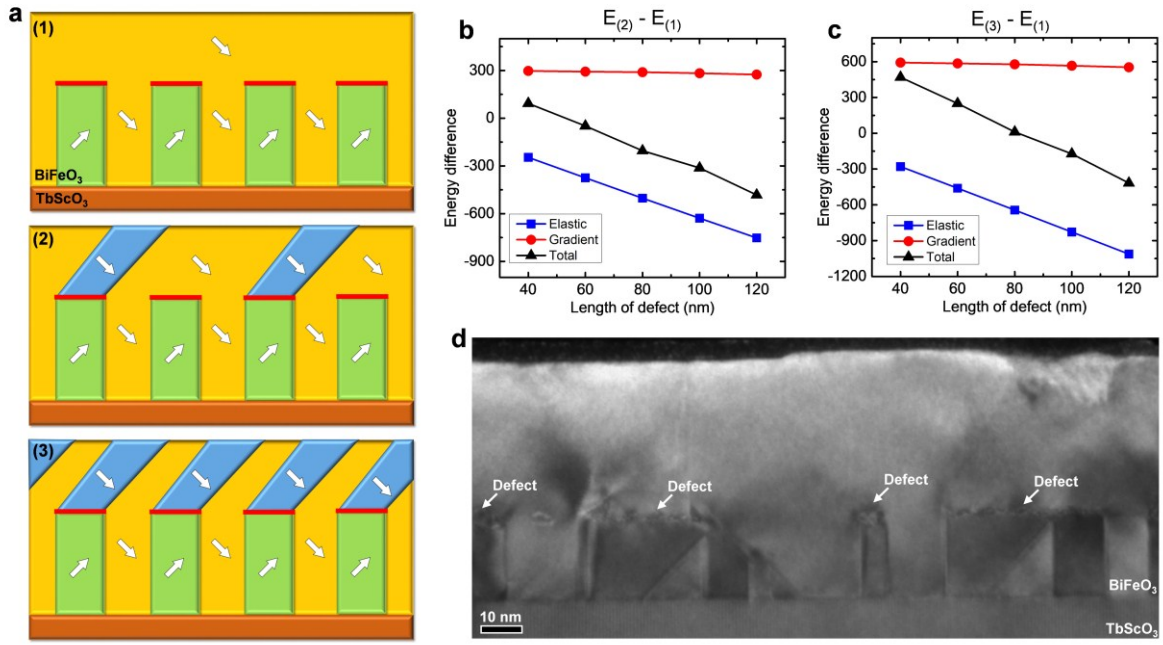

Figure 3. Energetic driving force for the domain transformation across the defects. **a**, Schematics of three metastable domain patterns modeled by phase-field simulations: (1) no 71° domains above the defect, (2) one 71° domain on every other defect, and (3) one 71° domain on each defect. The white arrows mark the polarization orientations. **b**, Calculated elastic, gradient, and total energy difference between domain patterns (2) and (1) shown in **a**. **c**, Calculated elastic, gradient, and total energy difference between domain patterns (3) and (1) shown in **a**. **d**, Cross-sectional dark-field TEM image of a 60 nm $BiFeO_3$ film, in which a larger monodomain and ordered 109° domains are separated by an array of defects.

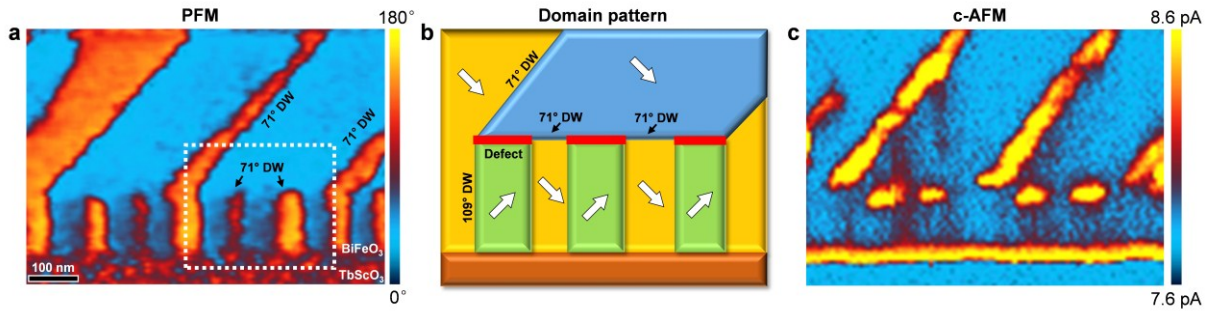

Figure 4. Conductive DW patterns stabilized by the defects. **a**, PFM phase image of a region in the 400 nm $BiFeO_3$ film containing ordered patterns of each 71° domain on five 109° domains. **b**, Schematic domain structures of the highlighted region in **a**. The white arrows mark the polarization orientations. **c**, Corresponding c-AFM map of the same region showing enhanced conductivity at inclined and horizontal 71° DWs. The current map was captured with a constant bias of 1.0 V applied between the tip and the sample. No domain switching or domain wall motion was observed after measuring the current.

Engineered structural defects are used as nano-building-blocks for configuring domain-wall patterns in multiferroic $BiFeO_3$ thin films. By utilizing the interaction between the polarization and the defects, two types of twinning domain structures are integrated into a single film without breaking the domain-wall periodicity.